

Emergence of Elastic Properties in a Minimalist Resilin-Derived Heptapeptide upon Bromination

Andrea Pizzi, Lorenzo Sori, Claudia Pigliacelli, Alfonso Gautieri, Clara Andolina, Greta Bergamaschi, Alessandro Gori, Pierre Panine, Antonio Mattia Grande, Markus B. Linder, Francesca Baldelli Bombelli, Monica Soncini, and Pierangelo Metrangolo*

This paper is dedicated to the victims of the COVID pandemic.

Bromination is herein exploited to promote the emergence of elastic behavior in a short peptide—SDSYGAP—derived from resilin, a rubber-like protein exerting its role in the jumping and flight systems of insects. Elastic and resilient hydrogels are obtained, which also show self-healing behavior, thanks to the promoted non-covalent interactions that limit deformations and contribute to the structural recovery of the peptide-based hydrogel. In particular, halogen bonds may stabilize the β -sheet organization working as non-covalent cross-links between nearby peptide strands. Importantly, the unmodified peptide (i.e., wild type) does not show such properties. Thus, SDSY(3,5-Br)GAP is a novel minimalist peptide elastomer.

into metabolites or even tissues is ubiquitous in both marine plants and animals,^[1] and exerts specific functions.^[2] Particularly intriguing is the case of the marine worm *Nereis*, whose jaws, in fact, contain halogenated tyrosines and histidines that are mainly localized at the outer surface of this functional component, forming a protective shell highly resistant to chemical and enzymatic attacks.^[3] More recently, bromine-rich tips of crab claws showed an elasticity modulus higher than calcified cuticles, resulting in remarkable fracture resistance.^[4]


Inspired by nature's examples of using biohalogenation to enhance chemical and mechanical properties of biomaterials,^[5,6] we have recently exploited halogenation of phenylalanine residues to enhance the aggregation propensity of short amyloidogenic sequences, for example, KLVFF and DFNKF, derived from amyloid β (A β)^[7] and human calcitonin (hCT), respectively.^[8] More recently, halogenation of tyrosine residues also proved to be effective in the supramolecular stabilization of highly polymorphic and structurally flexible peptide sequences,^[9–14]

inspired by nature's examples of using biohalogenation to enhance chemical and mechanical properties of biomaterials,^[5,6] we have recently exploited halogenation of phenylalanine residues to enhance the aggregation propensity of short amyloidogenic sequences, for example, KLVFF and DFNKF, derived from amyloid β (A β)^[7] and human calcitonin (hCT), respectively.^[8] More recently, halogenation of tyrosine residues also proved to be effective in the supramolecular stabilization of highly polymorphic and structurally flexible peptide sequences,^[9–14]

1. Introduction

Organisms living in particular habitats often find non-trivial solutions for adaptation, turning into an opportunity something that apparently is not. This is the case, for example, in the marine environment, where the high concentration of halide salts (especially chloride and bromide) in seawater has influenced the evolution of many species. Indeed, the inclusion of halogen atoms

A. Pizzi, L. Sori, C. Pigliacelli, C. Andolina, F. Baldelli Bombelli, P. Metrangolo
Laboratory of Supramolecular and Bio-Nanomaterials (SupraBioNanoLab)
Department of Chemistry, Materials, and Chemical Engineering "Giulio Natta"
Politecnico di Milano
Via Luigi Mancinelli 7, Milan 20131, Italy
E-mail: pierangelo.metrangolo@polimi.it
C. Pigliacelli, C. Andolina, P. Metrangolo
Hyber Center of Excellence
Department of Applied Physics
Aalto University
Puumiehenkuja2, Espoo FI-00076, Finland

 The ORCID identification number(s) for the author(s) of this article can be found under <https://doi.org/10.1002/smll.202200807>.

© 2022 The Authors. Small published by Wiley-VCH GmbH. This is an open access article under the terms of the Creative Commons Attribution License, which permits use, distribution and reproduction in any medium, provided the original work is properly cited.

DOI: 10.1002/smll.202200807

A. Gautieri, M. Soncini
Biomolecular Engineering Lab
Department of Electronics Information, and Bioengineering
Politecnico di Milano
Milan 20131, Italy
G. Bergamaschi, A. Gori
Istituto di Scienze e Tecnologie Chimiche – National Research Council of Italy (SCITEC-CNR)
Milan 20131, Italy
P. Panine
Xenocs SAS
1–3 Allée du Nanomètre, Grenoble 38000, France
A. M. Grande
Department of Aerospace Science and Technology
Politecnico di Milano
via La Masa 34, Milano 20156, Italy
M. B. Linder
Department of Bioproducts and Biosystems
School of Chemical Engineering
Aalto University
P.O. Box 16100, Aalto FI-00076, Finland

such as the $A\beta$ N-term region (i.e., DSGYEV), which is not fibrillogenic unless halogenated.^[15,16] In these systems, halogen atoms were found to boost their self-assembling capability enriching their interaction patterns with halogen bonds (XBs), that is, intermolecular interactions wherein halogen atoms function as electron acceptors.^[17] In particular, XBs usually take place between introduced halogen atoms and backbone amide oxygen of a close by peptide chain, thus strengthening the β -sheet structural core of amyloid fibrils known as the “steric zipper.”^[18] Given the capability of halogen atoms to promote supramolecular order in amyloidogenic peptides and the enhanced elastic moduli showed by brominated tissues of marine organisms, we moved to explore the possible induction of elastomeric properties in short peptides upon halogenation. Herein, we report the unprecedented emergence of such properties upon tyrosine bromination of a small peptide fragment (i.e., SDSYGAP; **Figure 1a**) derived from Resilin (Res), an elastomeric protein present in most insects, which features intrinsically disordered structure, unusual multi-stimuli responsiveness, and outstanding resilience^[18–20] (**Figure 1a,b**). This heptapeptide belongs to a consensus sequence of Exon-1, which is the domain providing high flexibility to the full-length protein (620 amino acids, aas).

In this frame, many efforts have been spent on the bio-synthesis of Res-like polypeptides (RLPs), endowed with both native Res regions and heterologous domains, to shape new properties for potential biomedical applications,^[21–23] including tissue engineering^[24] and drug delivery,^[25] as well as wearable sensors.^[26–29] RLPs’ elasticity arises from covalent cross-linking among polymer chains, which limits their extension and sliding, ensuring a complete shape recovery after deformation. Chemical cross-links occur by dityrosine bridges, which are formed enzymatically^[30] or using photochemical reactions.^[31]

Following a reductionist approach,^[32] that is, selecting a short peptide sequence characteristic of the chosen elastic protein, we, instead, propose a different design strategy for developing Res-based bioelastomers. In particular, we selected a Res consensus sequence of only seven aas, bearing a central tyrosine residue, in which both ortho positions to the tyrosine OH group have been brominated (**Figure 1b**), that is, two H atoms have been replaced by two Br atoms (see section Molecular Design in the Supporting Information). Tyrosine bromination promoted peptide self-assembly in a well-defined 3D network of fibrils, wherein XB plays a pivotal role in the structural stabilization of the self-assembled nanostructures, with the emergence of resilience in the peptide-based hydrogel (**Figure 1c**). Finally, our results also showed that, while the non-halogenated peptide SDSYGAP (**Res-Wt**) is intrinsically disordered, the brominated variant SDSY(3,5-Br)GAP (**Res-Br**) exhibited an elastomeric behavior, reminiscent of the properties of the parent protein.

2. Results and Discussion

The self-assembly behavior of the brominated Res-based sequence chosen for this study, that is, SDSY(3,5-Br)GAP, was directly compared with that of the unmodified peptide (SDSYGAP) (**Figure 1b**). Both **Res-Br** and **Res-Wt** were extremely soluble in water as expected since the parental Exon I sequence of Res is highly hydrophilic.^[25]

Circular dichroism (CD) spectra of 10 mM aqueous solutions of the two peptides revealed the signature of a polyproline II (PPII) conformation,^[33] which is typical of peptide elastomers and consists of an intense negative band in the 190–200 nm range (**Figure S13**, Supporting Information). A small red shift

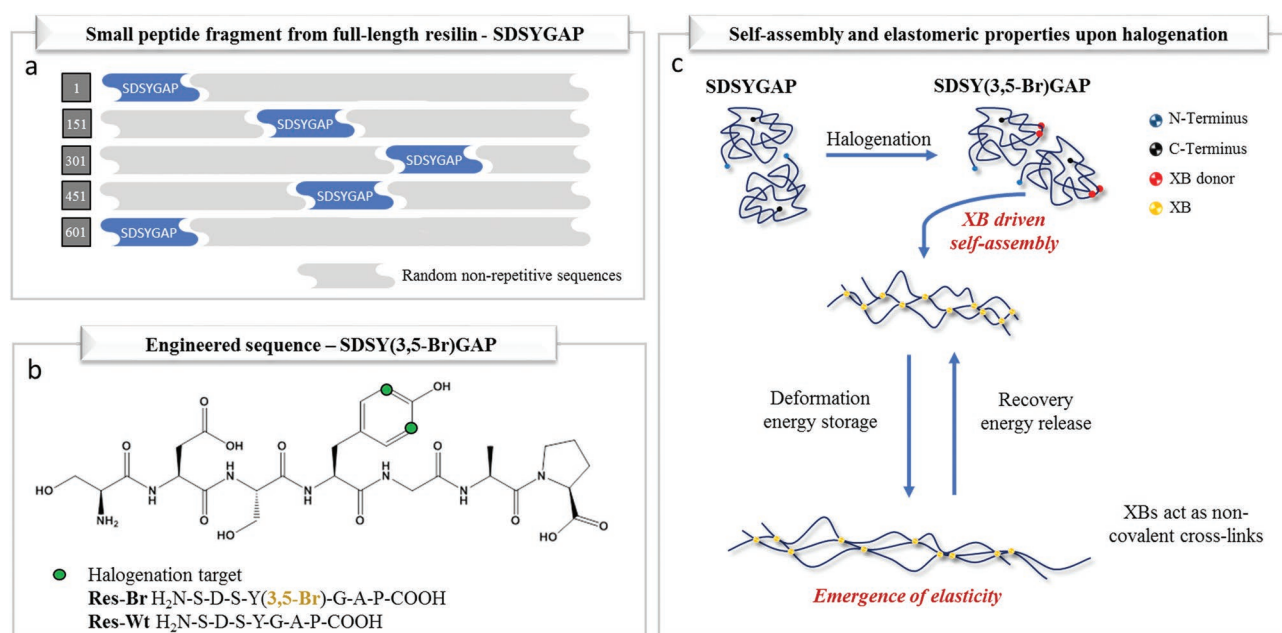


Figure 1. a) Schematic representation of the SDSYGAP sequence repetition in a full-length Resilin protein. b) Chemical structure of SDSY(3,5-Br)GAP (**Res-Br**) and SDSYGAP (**Res-Wt**). Bromine atoms replaced the H atoms at the ortho positions to the OH group of the tyrosine ring. c) Cartoon representation of XB-driven SDSY(3,5-Br)GAP self-assembly and the emergence of elastic properties.

of the negative peak in the CD spectrum with respect to that of **Res-Wt** suggested a possible role of bromine in altering the $\pi \rightarrow \pi^*$ charge-transfer transition^[34] related to the peptide bond.

Res-Br exhibited a critical gelation concentration (CGC) of 200 μM , that is, 14 wt%, in water (Figure 2a) as expected for such a hydrophilic sequence with free N and C termini,^[35] in which bromination is the unique point mutation. Of note, the native peptide does not form a gel at any concentration, indicating an important role of bromination in the self-assembly behavior of this system. Transmission electron microscopy (TEM) and scanning electron microscopy (SEM) images showed that the hydrogel formed by **Res-Br** (Figure 2b,c) consisted of an entangled network of fibrils with a cross-section of 140 ± 10 nm, in agreement with the typical features observed in amyloid supramolecular hydrogels.^[36] Polarized light optical microscopy (POM) revealed that the **Res-Br** hydrogel was characterized by a supramolecular order showing typical birefringence (Figure S14, Supporting Information), which was not, instead, observed for 200 μM **Res-Wt** solutions, only showing the formation of amorphous aggregates by TEM imaging (Figure S15, Supporting Information).

Res-Br hydrogels were fully thermoreversible. The differential scanning calorimetry (DSC) profile of the 200 μM hydrogel presented a broad endothermic transition at about 24 °C, consistent with peptide solubilization, hence disassembly of the fibrillar supramolecular architecture (Figure S16, Supporting Information). Reversible gel formation on cooling was demonstrated by an exothermic signal at about 16 °C. Thermal transitions observed by DSC were confirmed through POM combined with a temperature-controlled stage and also through dynamic light scattering (DLS) (Figure S17, Supporting Information). Specifically, it was possible to observe at the POM that the birefringent network of fibrils, forming the hydrogel, progressively dissolved upon heating, with the formation of a transparent solution showing a homogeneous isotropic phase. This solution yielded back a homogeneous fibrillar network upon cooling. On the other side, the 200 μM **Res-Wt** solution did not display any of these thermal transitions in the same temperature range, remaining an isotropic liquid.

Small-angle X-ray scattering (SAXS) and wide-angle X-ray scattering (WAXS) experiments of 200 μM **Res-Br** hydrogels and **Res-Wt** solutions were performed at different temperatures

(10 and 20 °C, below and close to the sol–gel transition, respectively). **Res-Br** hydrogels showed a very complex scattering profile in the whole investigated temperature range, consistent with highly ordered structures. The SAXS/WAXS datasets, shown in Figure 3a,b exhibit three principal hierarchical organization levels. At the atomic scale, for q values among $1\text{--}4 \text{ \AA}^{-1}$ (Figure 3b), four distinct peaks at 1.33, 1.43, 1.55, and 1.73 \AA^{-1} are visible. The observed pattern is consistent with a structural order typical of an amyloid cross- β architecture,^[37] namely multiple intense signals in the range $3.6\text{--}4.7 \text{ \AA}$ arising from the characteristic spacing^[14] between hydrogen-bonded β -strands within β -sheets. Of note, the **Res-Br** freeze-dried hydrogel displays Fourier transform infrared spectroscopy (FTIR) peaks consistent with β -sheet architecture (Figures S18 and S19, Supporting Information), hence supporting the SAXS results. Interestingly, the same SAXS peaks were observed in the powder X-ray diffraction (PXRD) pattern of the freeze-dried gel of the same sample (Figure 3c). In the PXRD diffractogram, a less pronounced peak, centered at about 11 \AA is also visible, probably related to the distance between facing β -sheets running perpendicular to the same fiber axis, usually identified as the “steric zipper” motif.^[38] At the medium q -range in the SAXS curve, a shoulder is visible at $q = 0.224 \text{ \AA}^{-1}$ (see inset of Figure 3a). This shoulder is related to a characteristic distance in the system of $\approx 27 \text{ \AA}$. Finally, the low- q part exhibits a very clear oscillatory pattern with deep local minima at $q^* = 0.009, 0.022, 0.037, 0.052, \dots \text{ \AA}^{-1}$, with a periodicity $\Delta q = 0.014 \text{ \AA}^{-1}$. It is worth noting that this regular modulation is visible up to the medium q -range of 0.3 \AA^{-1} , reinforcing the picture of a material with a high level of organization over a very large domain size. The small q -value oscillatory part of the SAXS dataset is very well-resolved and is the signature of a narrow dispersion in size of large dimension objects with relatively sharp interfaces and well-defined in space. Moreover, the presence of a four-leaf pattern, visible in the 2D data, recalls structure patterns along cylindrical scattering entities such as those already encountered in the literature.^[39] The 2D SAXS pattern (Figure 3d) shows regular Debye rings from a well-defined nanostructure with additional reinforcement of signal at a particular azimuth, revealing the presence of an anisotropic contribution, as observed on the first Debye ring at $q^* = 0.014 \text{ \AA}^{-1}$ and clearly depicted on the $I(\Psi)$ plot (inset of Figure 3d). This could

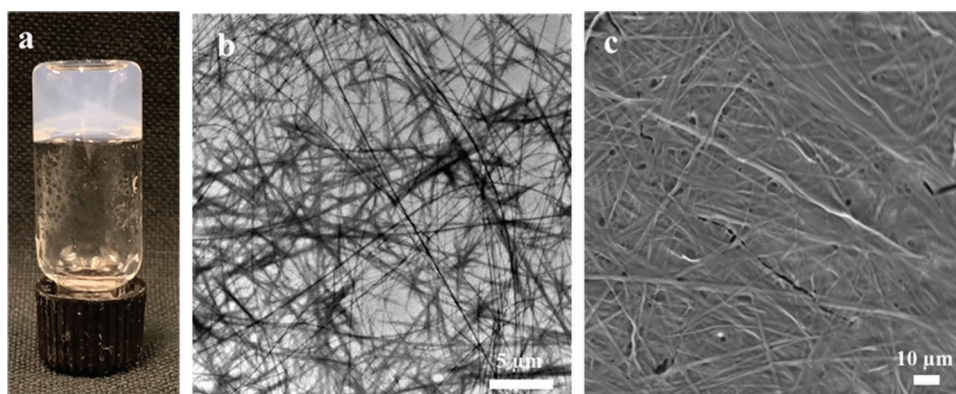


Figure 2. a) 200 μM aqueous sample of **Res-Br**; different concentrations have been evaluated (see sample preparation in ESI); b) TEM image of the halogenated hydrogel (100 μM , dilution from 200 μM). c) SEM image of 200 μM hydrogel formed by the halogenated peptide.

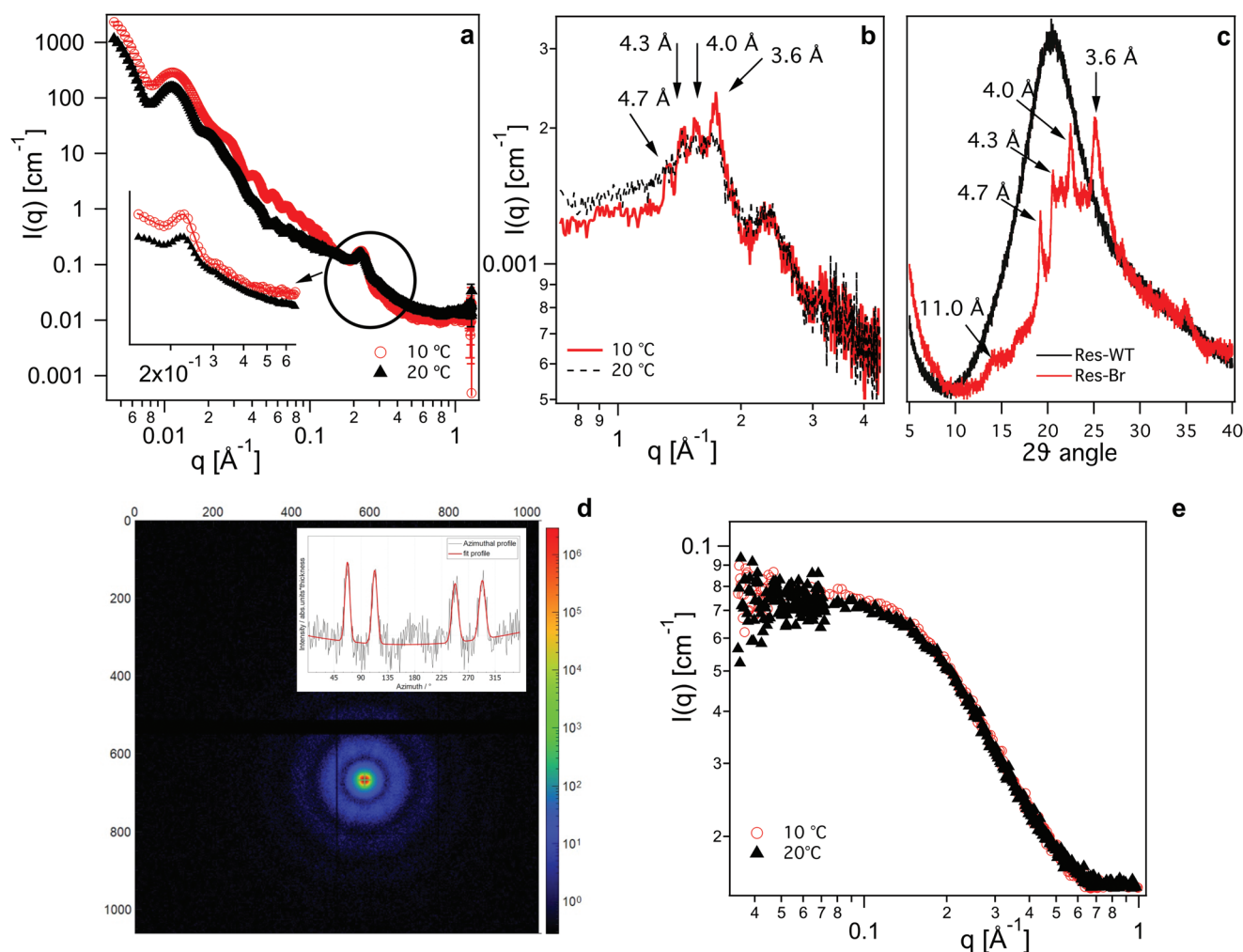


Figure 3. a) SAXS 1D data of 200 mM **Res-Br** peptide gel at 10 °C (red) and 20 °C (black). The lower inset shows an enlargement of the peak observed at $q = 0.227 \text{ \AA}^{-1}$ and 10 °C data is offset by ($\times 2$) for clarity. b) WAXS 1D data of 200 mM **Res-Br** peptide gel at 10 °C (red) and 20 °C (black). c) PXRD pattern of 200 mM freeze-dried **Res-Br** hydrogel (red) and **Res-Wt** solution (black). d) SAXS/WAXS 2D data of 200 mM **Res-Br** peptide gel at 20 °C. Some anisotropy of SAXS data at first-order Debye ring $q^* = 0.014 \text{ \AA}^{-1}$ is shown in the inset. First-order Debye ring exhibits, as plotted along azimuth ψ for $\langle q^* \rangle$, a typical 4-leaf spots at $\psi = 67^\circ, 112^\circ, 247^\circ$, and 293° . e) SAXS curves of 200 mM **Res-Wt** solutions at 10 °C (red) and 20 °C (black).

be attributed to the correlation of two populations of fibers, inclined to each other by 45° from the vertical axis. Considering the capillary being vertical, since most of the sample is not exhibiting a preferential orientation, a not negligible population of fibers is aligned along the vertical axis with a tilt of $\pm 22.5^\circ$. Importantly, the scattering profile of a 200 mM solution of **Res-Wt** (Figure 3e) is typical of unstructured (globular) proteins,^[40] fully coherent with the other experiments, and with the PXRD pattern of its freeze-dried solution, which is typical of an amorphous solid (Figure 3c).

To get more insights into the supramolecular organization of the formed peptide fibers and relate these distances to molecular structural parameters,^[41] molecular dynamics (MD)^[42] was employed to model the possible structures formed by **Res-Br** and **Res-Wt**. Based on the characteristic Bragg peaks of cross- β architecture found by PXRD and WAXS, eight different fibril-like configurations were modeled and their structural stability was assessed over time. The starting fibril models were identified with a three-letter code, each referring

to three different packing parameters: type of β -sheet (Parallel/Antiparallel), reciprocal orientation between facing β -sheet (Parallel/Antiparallel), and termini orientation (C-to-N termini or C-to-C) between sheets interacting laterally (Figure S21, Supporting Information). Fibrils formed by **Res-Wt** are unstable, as suggested by the root mean square deviation (RMSD) that increases with time (Figure 4a). Instead, halogenation makes stable the fibrils formed by **Res-Br**, since all the tested configurations have a low RMSD that reaches a plateau within a few nanoseconds (Figure 4b). This suggests that the brominated sequence forms very stable assemblies also reflecting a higher β -sheet content compared to the unmodified peptide (Figure S22, Supporting Information).

Among tested fibril configurations, the most stable is the PAN (Parallel, Antiparallel, C-to-N) for both peptides. The analysis of the structures at the end of the MD simulations indicates that **Res-Wt** protofibrils form unordered amorphous structures (Figure 4c), progressively losing peptide molecules from the fibril surface, and showing reduced β -sheet content

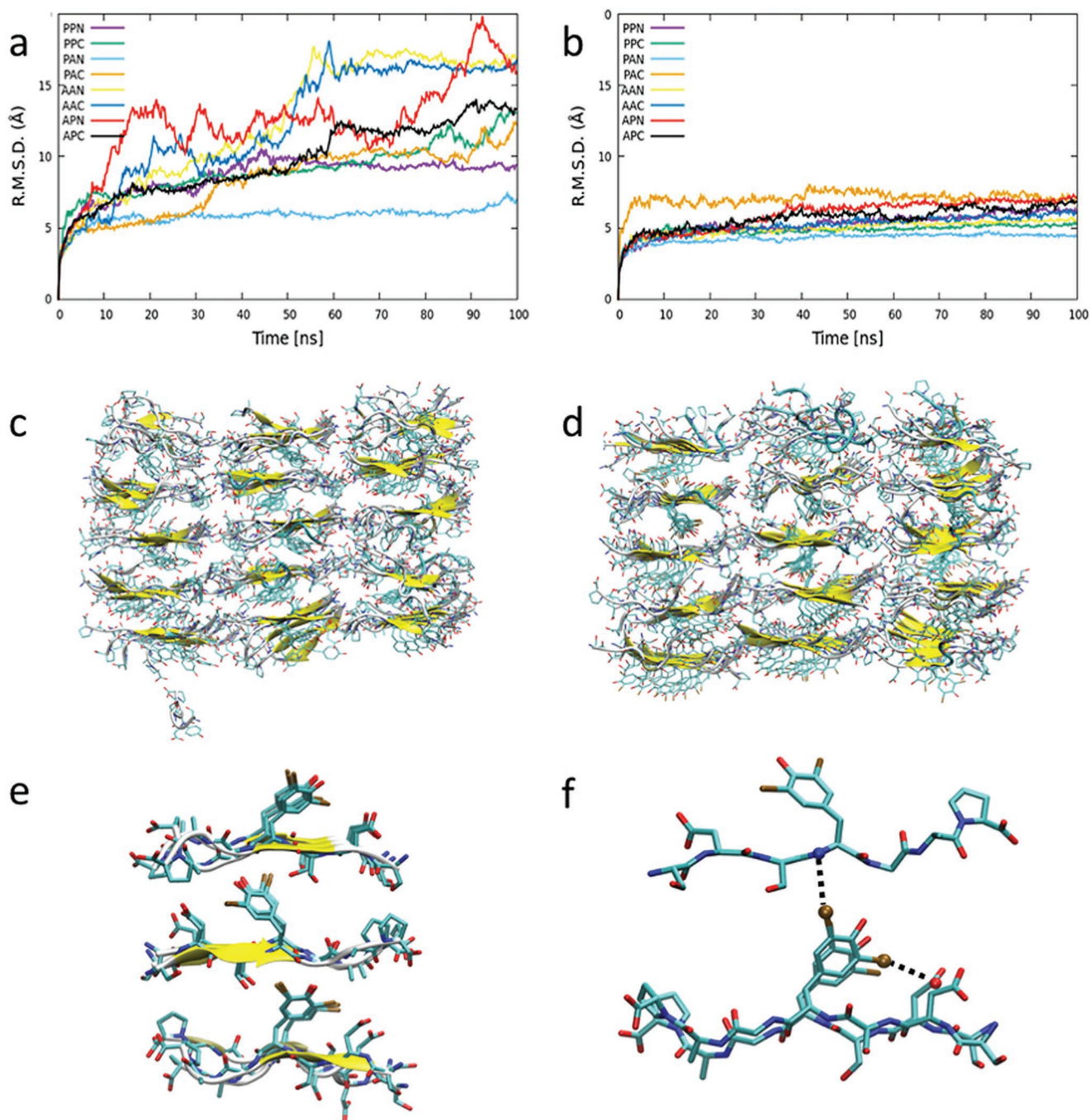


Figure 4. a) Root mean square deviation of the protofibril models made of the unmodified peptide (**Res-Wt**). b) Root mean square deviation of the protofibril models made of the halogenated peptide (**Res-Br**). c) Final structure (at the end of 100 ns MD) of the wild-type peptide PAN fibril and d) of the halogenated peptide PAN fibril. The wild-type peptide forms an unstructured aggregate, whereas the halogenated peptides present ordered fibrils. In **Res-Wt** the protofibril appears less ordered than the **Res-Br** protofibril, in particular showing the lack of a clear pattern of lateral intermolecular interactions. e) **Res-Br** packing stabilized by a network of hydrogen bonds, highlighted as black dotted lines in (f). The molecules, represented in capped sticks mode, were extracted from the last frame of the MD simulations relative to the PAN configuration of the **Res-Br** peptides. The bromine atoms forming halogen bonds are depicted as spheres (color code: light blue, carbon; red, oxygen; blue, nitrogen; brown, bromine; hydrogen atoms have been omitted for clarity).

(Figure S22c, Supporting Information) and a lower number of hydrogen bonds (Figure S22c, Supporting Information). Although a majority of the peptides do not lose contact with each other, there are no consistent stabilizing interactions

throughout the fibril. Conversely, the brominated peptide forms ordered fibrils (Figure 4d) stabilized by several non-covalent interactions. Indeed, in the PAN configuration, parallel β -sheets of **Res-Br** are stabilized by up to five hydrogen bonds involving

the amide groups of the peptide backbone, in addition to intermolecular $\pi \cdots \pi$ stacking between paired 3,5-di-bromo-Tyr rings (Figure 4e). Of note, bromine atoms exert a key role in strengthening peptide self-assembly thanks to halogen bonds (XBs) (Figure 4f).

As it is non-trivial to give unambiguous values of distances and angles to describe a non-covalent interaction in an MD simulation, the possible XBs were identified on basis of time occupancy, that is, the percentage of simulation time (calculated on the last 50 ms of computation) in which two atoms comply with predetermined criteria of angles and distances. Here, were considered as XBs the interactions involving bromine atoms with a distance lower than the sum of the van der Waals radii of the involved atoms and for which C-Br \cdots D angle (where D is a nucleophilic atom) was comprised between 160° and 180°. Using these criteria, XBs between the side chain of 3,5-di-bromo-Tyr and backbone nitrogen of facing strands (time occupancy 25.2%) were detected. A similar XB (time occupancy 14.7%) occurs between bromine and backbone amide oxygen of facing strands. Importantly, the most relevant XB (time occupancy 61.3%) is observed between bromine atoms of the tyrosine residue and oxygen atoms of the aspartate side chain from a stacked strand. Overall, halogen atoms reinforce the peptide's structural packing both parallelly and orthogonally to the fibril axis, conferring higher supramolecular order to the studied sequence, that is, originally, mainly amorphous. In detail, intramolecular XBs reduce the conformational freedom of peptide molecules, stabilizing the β -sheet structure. Regarding inter-sheet XBs, they act as non-covalent cross-links that reduce the sliding of interacting sheets upon shear stress, hence preserving the overall supramolecular structure. Concerning lateral packing, sided peptides form salt bridges involving N and C termini. Looking into the features of the fibrils formed by **Res-Br**, the intra-strand distance is 5.1 ± 0.2 Å, while the inter-sheet distance among facing β -sheets is 9.5 ± 0.2 Å, consistent with the crystal structures of small amyloidogenic peptides previously reported.^[38] Thus, we can hypothesize that the characteristic distance of 27 Å obtained by SAXS, might be related to the cross-section of amyloid protofibrils formed by stacked β -sheets forming the mature fibrils.

Given the high supramolecular ordering of **Res-Br** in the hydrogel state driven by non-covalent interactions involving bromine atoms, the macroscopic properties of **Res-Br** hydrogels were also assessed, through rheological and compression tests.^[7] 200 and 500 mM **Res-Br** hydrogels were analyzed at a controlled temperature below the gel-sol transition threshold (i.e., <20 °C).

Frequency sweep experiments (Figure 5a) indicate a clear predominance of the elastic component ($G' > G''$) for both tested samples. Specifically, the 500 mM sample has an elastic shear modulus in the range 10^5 – 10^6 Pa, while 200 mM gel shows an expected lower G'' value (10^4 – 10^5 Pa). The elastic modulus decreases with temperature, consistently with progressive weakening of the gel network upon approaching sol transition. Above this limit (sweep frequency test at 30 °C), the crossover between G' and G'' was observed, indicating a predominant viscous behavior of the material. Notably, samples of **Res-Wt** at the same concentrations are clear liquids, showing viscous behavior in every tested condition (Figure S23, Supporting

Information). The step test was performed to describe the regeneration of the material after deformation (Figure 5b,d). In detail, the hydrogel was subjected to 0.01% strain for 2 min and subsequently to a 1% strain for another 2 min; this cycle was repeated twice. In the recovery interval, the elastic modulus (G') is immediately above the viscous modulus (G'') showing a rapid and almost total recovery of the structure (and of the elastic response). Compression tests (Figure S24, Supporting Information) were performed only on **Res-Br**; here, the hydrogels were subjected to axial strain, and the mechanical response of the material was recorded in continuous mode. Both tested hydrogels showed valuable recovery after compression loading, clearly demonstrating the elastic response of the self-assembled peptide network. Of note, these compression tests are complementary to the step tests, and the former reasonably allows to infer that the observed behavior of the hydrogel is consistent with an elastic response. Indeed, a viscous material would not be able to display even a partial recovery after compression. To the best of our knowledge, this is the first example of elastomeric properties emerging in such a short peptide upon introduction of halogen atoms. In previous research, we showed that halogen atoms could exacerbate a property or behavior that is already observable in the corresponding non-modified peptide.^[8] Here, instead, halogenation induced the emergence of a property, that is, elasticity, which is encoded in the parent protein, that is, resilin, although not expressed in the wild-type peptide sequence. As demonstrated by MD simulations, bromine atoms have a key role in the elasticity of the hydrogel, working in synergy with other non-covalent interactions and acting as physical cross-links that ensure stress recovery. Notably, 200 mM hydrogels of **Res-Br** displayed elastic behavior even after overpassing the yielding, which suggests self-healing properties of the peptide network. In this regard, qualitative experiments also confirm this property (Figure S25, Supporting Information).

3. Conclusion

In conclusion, we reported that the bromination of tyrosine residues in a small heptapeptide derived from resilin—SDSYGAP—determines the emergence of elastic properties that are not observable in the non-halogenated sequence. Bromine atoms promote the occurrence of a network of intermolecular interactions that enhance peptides' self-assembly. In particular, halogen bonds may stabilize the β -sheet organization working as non-covalent cross-links between nearby peptide strands, as suggested by MD simulations. Elastic and resilient hydrogels are obtained, which also show self-healing behavior, thanks to the promoted non-covalent interactions that limit deformations and contribute to the structural recovery of the peptide-based hydrogel. Thus, **Res-Br** can be identified as a novel minimalist peptide elastomer.^[43] The appearance of elastomeric properties in such a short peptide is remarkable and even more surprising is the fact that such a huge structural and functional change is induced by only replacing two H atoms with two Br atoms. Importantly, the unmodified peptide (i.e., wild type) does not show such properties. **Res-Br** ease of synthesis, scalability, and biocompatibility paves the way for the development of a

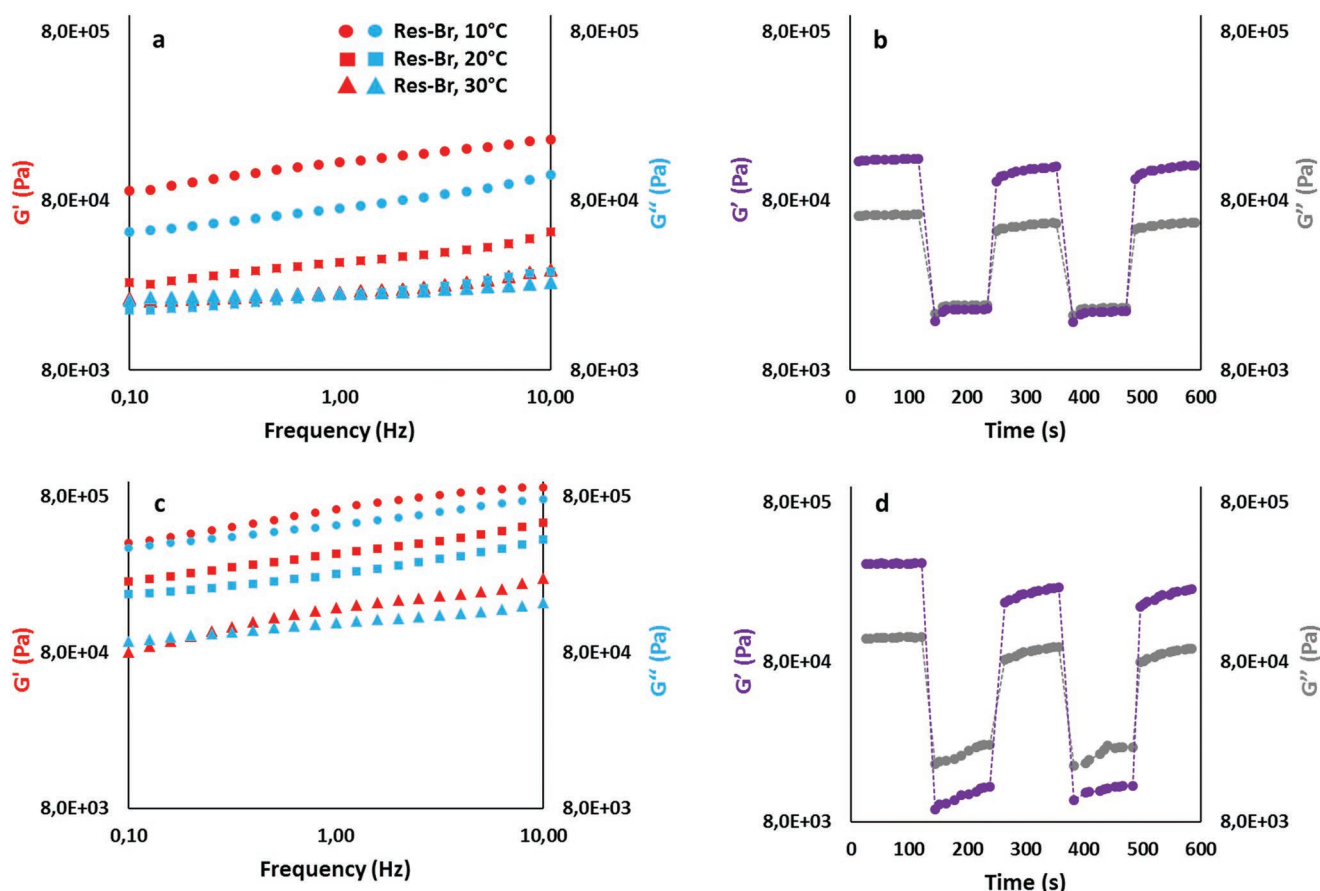


Figure 5. Frequency sweep test on a) 200 mm and c) 500 mm **Res-Br** hydrogels. Step test on b) 200 mm and d) 500 mm **Res-Br** hydrogels revealing the elastic behavior of the self-assembled peptide network. In the step test, the hydrogel was subjected to i) 0.01% strain for 2 min and then to ii) 1% strain for 2 min. This cycle was repeated twice.

totally new class of bioelastomers. Elastomeric compositions of **Res-Br** with other biomaterials are under current investigation and will be reported elsewhere.

4. Experimental Section

Materials: Peptides with confirmed amino acid analysis (purity $\geq 98\%$) were purchased from Biofab Research (Rome, Italy). The integrity of peptides was verified by ion spray mass spectrometry and their purity was determined by reverse-phase high-pressure liquid chromatography (HPLC).

Sample Preparation: Peptide solutions/hydrogels were prepared by dissolving each peptide in deionized water (18.2 M Ω cm). Glass vials containing peptide solutions were sealed, sonicated for 20 s, and gently heated in a water bath at 40 °C for 5 min, before slow cooling to 20 °C. The hydrogel was formed within a few minutes. All samples were stored at r.t. for 48 h before analysis. The CGC was determined by investigating samples ranging from 5 to 500 mm (5/10/50/150/200/500 mm) on the basis of the vial inversion test and resulted to be 200 mm.

Reverse Phase High-Pressure Liquid Chromatography: HPLC grade acetonitrile (ACN) and ultrapure 18.2 Ω water (Millipore-MilliQ) were used for the preparation of all buffers for liquid chromatography. The chromatographic columns were from Phenomenex (Torrance CA, USA). HPLC eluent A: 97.5% H₂O, 2.5% ACN, 0.7%TFA; HPLC eluent B: 30% H₂O, 70% ACN, 0.7%TFA.

RP-HPLC Analysis and Purification: Analytical RP-HPLC was performed on a Shimadzu Prominence HPLC (Shimadzu) using a Shimadzu Shimpack GWS C18 column (5 microns, 4.6 mm i.d. \times 150 mm). Analytes were eluted using a binary gradient of mobile phase A (100% water, 0.1% trifluoroacetic acid) and mobile phase B (30% water, 70% ACN, 0.1% trifluoroacetic acid) using the following chromatographic method: 100% B/A to 50% B/A in 14 min; flow rate, 1 mL min⁻¹.

Nuclear Magnetic Resonance: Nuclear magnetic resonance (NMR) spectra were recorded at (300:3) K on a Bruker Avance III 400 MHz spectrometer equipped with a 5 mm QNP probe (¹⁹F-³¹P-¹³C/¹H); chemical shifts were reported in ppm downfield from SiMe₄, with the residual proton (CHCl₃: $d = 7.26$ ppm, THF: $d = 1.73$ ppm) and carbon (CDCl₃: $d = 77.0$ ppm, THF: $d = 25.37$ ppm) solvent resonances as internal references. Proton and carbon assignments were achieved by means of ¹³CAPT, ¹H-¹H COSY, and ¹H-¹³C HSQC experiments.

Electrospray Ionization Mass Spectrometry: The electrospray ionization mass spectrometry (ESI-MS) experiments were performed using a Bruker Esquire 3000 PLUS (ESI Ion Trap LC/MSn System), equipped with an ESI source and a quadrupole ion trap detector (QIT). The acquisition parameters were: needle: 4.5 kV, nitrogen flow rate: 10 L h⁻¹, cone voltage: 40 V, scan resolution and range: 13 000 (m/z) s⁻¹ over the mass range m/z 35–2000, by direct infusion of the photo-irradiated solutions at a rate: 4 μ L min⁻¹. The assignment of some detected species was confirmed by collision-activated decomposition (CID) mass spectrometry experiments (MS²).

Circular Dichroism: All the CD experiments were carried out in deionized water (18.2 M Ω cm) in 1 mm pathlength quartz cuvettes, using

a JASCO J-815 CD spectrometer. Acquisitions were performed between 190 and 250 nm with a 0.1 nm data pitch, 1 nm bandwidth, 100 nm min⁻¹ scanning speed, and 1 s response time. All the spectra were an average of 10 scans and were corrected from a reference solution, that is, deionized water alone. Raw data (θ , in mdeg) were subsequently converted to mean residue ellipticity ($[\theta]$ in deg cm² dmol⁻¹).

Electron Microscopy: TEM bright-field images were acquired using a Philips CM200 electron microscope operating at 200 kV equipped with a Field Emission Gun filament. A Gatan US 1000 CCD camera was used and 2048 × 2048 pixels images with 256 grey levels were recorded. Some other images were recorded with a DeLong Instruments LVEM5, equipped with a field emission gun and operating at 5 kV. Peptide samples were placed onto a 200-mesh carbon-coated copper grid and air-dried for several hours before analysis. No negative staining was used. The sample of the peptide was prepared for morphological analysis by SEM. The sample was collected on a stub and coated with a conductive thin layer (using sputtering of gold) to make them conductive. The analysis was performed using a SEM Zeiss EVO 50 EP.

Polarized Light Optical Microscopy: POM images were registered with a Leica DM4500P POM system that was equipped with a Canon EOS 60D camera. The sol–gel transition temperature of Res-Br was determined using the optical microscope combined with a Linkam Scientific temperature-controlled stage.

Powder X-Ray Diffraction Analysis: PXRD measurements were performed with a Bruker AXS D8 powder diffractometer, with experimental parameters as follows: Cu-K α radiation ($\lambda = 1.54056 \text{ \AA}$), scanning interval 5–40° at 2θ , step size 0.009°, exposure time 1.5 s per step. The molecular structure of the samples, that is, the d -spacing can be determined using Bragg's law: $n\lambda = 2d\sin\theta$, where n is an integer number, λ is the wavelength of the incident X-ray beam, and θ is the scattering angle. Powdered samples were analyzed using a silicon-film glass slide as a sample holder.

Differential Scanning Calorimetry: DSC analyzes were performed with a Mettler Toledo DSC823e calorimeter using 40 μ L aluminum crucibles for the samples. Mettler STARe software was used for data analysis. The heating step was recorded from 5 to 30 °C at a 1 °C min⁻¹ heating rate; the cooling step was from 30 to 5 °C and –1 °C min⁻¹ cooling rate.

Quantum Mechanical Calculations: Quantum mechanical (QM) calculations for di-Br-Tyr were performed using Gaussian09 software.^[44] The model molecule was optimized using density functional theory (DFT) by employing the hybrid B3LYP exchange-correlation functional^[45] and the aug-cc-pVTZ basis set on all the atoms. Prior to the computation of the electrostatic potential, a tight optimization was carried out to obtain a very accurate minimum energy molecular geometry.

Parametrization of Halogenated Amino Acids: In order to correctly represent the σ -hole on the halogen atoms of the di-Br-Tyr residue, the AMBER14sb force field^[46] was modified by introducing positively charged extra particles (EPs), following the method described in previous work.^[42] Atomic partial charges were evaluated using the restrained electrostatic potential (RESP) approach.^[47] The two EPs were positioned at an initial distance Br-EP of 1.5 Å and with a C ζ -Br-EP angle of 180°. Initial RESP charge calculations for halogenated amino acids showed that the EP atom presented a positive charge whose magnitude depended on the Br-EP distance. The optimal Br-EP distances (and consequently EP charges) were then obtained by testing different distances until the error in the electrostatic potential reached a minimum (Figure S21, Supporting Information). Spring constants for bond and angle terms were taken from ref. ^[48]. Table S1, Supporting Information, in ESI presents the most relevant parameters for the modified di-Br-Tyr amino acid.

Molecular Dynamics Simulations: The initial structure of the SDSYGAP peptide was generated with Pymol,^[49] while the protofibril molecular models were generated using VMD.^[50] The protofibrils using 3 × 5 × 8 peptides, for a total of 120 peptides were generated. The fibrils were made using different possible configurations in order to screen possible peptides' different packing, namely: parallel or antiparallel β -sheets, parallel or antiparallel strands, C-to-N termini, or C-to-C termini (Figure S12b, Supporting Information). This resulted in a total of eight different protofibrils made with the wild-type peptide. The different configurations

were named with a three-letter code, where the first letter referred to the type of the β -sheet (Parallel/Antiparallel), the second letter referred to the orientation of the strands (Parallel/Antiparallel), and third letter referred to the termini orientation (C-to-N termini or C-to-C). Finally, in order to generate the halogenated protofibrils, all tyrosine amino acids were substituted with the di-Br-Tyr model. All molecular models were solvated with ≈ 25000 TIP3P water molecules and 120 Na⁺ ions were added in order to neutralize the system. The set-up resulted in systems of ≈ 80000 atoms in a simulation box of initial dimensions of $\approx 90 \times 90 \times 120 \text{ \AA}^3$. The systems were simulated following protocols described in previous studies.^[42,51,52] All systems were minimized and equilibrated for 100 ps using the NAMD code^[53] under constant pressure and temperature (NPT) conditions in order to relax the volume of the periodic box. The pressure was set to 1 atm and the temperature to 300 K while using a time step of 2 fs, a nonbonded cut-off of 12 Å, rigid bonds, and particle-mesh Ewald long-range electrostatics. During minimization and NPT equilibration, the C α atoms of the peptides were restrained by a 10 kcal mol⁻¹ Å⁻² spring constant to prevent peptide diffusion. Subsequently, the production run was performed using ACEMD^[54] on an NVIDIA Kepler K40 GPU for a total time of 100 ns. A longer time step of 4 fs was used thanks to the hydrogen mass repartitioning scheme implemented in ACEMD. All other parameters (temperature, nonbonded cut-off, and PME) were kept the same as in the equilibration phase. The stability and the evolution of the systems were assessed by monitoring the RMSD of the C α . The analyses were performed with in-house tcl-scripts^[51,55,56] in VMD.^[50] The halogen bonds were defined on a geometric basis, where the distance between the halogen atom and the halogen bond acceptor was <4.0 Å, and the angle formed by the carbon atom, the halogen atom, and the halogen bond acceptor was >140°.

Small-Angle X-ray Scattering: X-ray scattering measurements at 200 mm were performed at SAXSLab Sapienza with a Xeuss 2.0 Q-Xoom system (Xenocs SA, Sassenage, France), equipped with a micro-focus Genix 3D X-ray source ($\lambda = 0.1542 \text{ nm}$), a 2D Pilatus3 R 300K detector, which could be placed at a variable distance from the sample, and an additional Pilatus3 R 100K detector at a fixed shorter distance from the sample to access larger scattering angles (Dectris Ltd., Baden, Switzerland). Beam size was defined through the two-pinhole collimation system equipped with “scatterless” slits to be 0.5 mm × 0.5 mm. Calibration of the scattering vector q range, where $q = (4\pi \sin\theta)/\lambda$, 2θ being the scattering angle, was performed using silver behenate. Measurements with different sample-detector distances were performed so that the overall explored q region was 0.045 nm⁻¹ < q < 1.25 nm⁻¹. Subsequently, on the sample at 150 mm, complementary measurements were performed with a Xeuss 3.0 UHR SAXS/WAXS system (Xenocs SAS, Grenoble, France) equipped with a GeniX 3D Cu K alpha radiation source ($\lambda = 1.54 \text{ \AA}$) and a Q-Xoom in-vacuum motorized Eiger2 R 1M detector (Dectris Ltd., Switzerland) for data collection. Samples were loaded into disposable borosilicate glass capillaries with a nominal thickness of 1.5 or 2.0 mm and sealed with hot glue before placing them in the instrument sample chamber at reduced pressure ($\approx 0.2 \text{ mbar}$) in thermostatic holders. 2D scattering patterns were subtracted for the “dark” counts, and then masked, azimuthally averaged, and normalized for transmitted beam intensity, exposure time, and subtended solid angle per pixel, by using the Foxtrot software developed at SOLEIL. 1D I versus q profiles were then subtracted for the solvent and capillary contributions and put in absolute scale units (cm) by dividing the sample thickness estimated by scanning the capillary with the X-ray beam. The different angular ranges were merged using the SAXS utility tool.^[57] Data set collected at Xenocs headquarters were processed as follows: 2D data reduction into 1D plots of scattering intensities $I(q)$ as a function of momentum transfer, q ($q = 4\pi \sin \theta/\lambda$, θ is half the scattering angle) was performed automatically using Xenocs XSACT software. Data analysis was performed using Xenocs XSACT software (data reduction, azimuthal profile, average, subtract, merge, peak fit, and polar representation modules).

Rheology: Dynamic rheological measurements were performed on a rheometer AR2000ex (TA Instruments) equipped with a temperature-controlled Peltier plate. A 25 mm parallel plate geometry was employed

for all the measurements and sample thickness was fixed at 500 μm . The linear viscoelastic region was verified by means of a strain sweep test at 1 Hz. Frequency sweep experiments (0.01–10 Hz) were carried out in the small-amplitude range (0.05% strain) in a temperature range from 10 to 30 $^{\circ}\text{C}$. Compression tests were also performed on the same instrument used in axial mode at 10 $^{\circ}\text{C}$. Samples were squeezed at 1 $\mu\text{m s}^{-1}$ up to a distance of 25 and 50 μm . Loading and unloading forces were recorded.

Self-Healing Test: For the evaluation of the self-healing properties, two 200 mm samples of **Res-Br** in MilliQ water were prepared. A blue dye was added during the preparation of one of the samples. After gelation, the hydrogels were placed in circular molds, obtaining two disc-shaped samples. These discs were cut in half and joined together by matching the two halves. Self-healing behavior was assessed at a controlled temperature ($T = 20^{\circ}\text{C}$) using a temperature-controlled stage combined with an optical microscope, registering progressive changes at the joint.

Fourier Transform Infrared Spectroscopy: Infrared spectra were recorded at room temperature using a Nicolet iS50 FT-IR spectrometer equipped with a DTGS detector. Freeze-dried 200 mm peptide samples were analyzed in ATR mode. Spectra represent an average of 64 scans recorded in a single beam mode with a 2 cm^{-1} resolution and corrected for the background.

Dynamic Light Scattering: DLS experiments were performed on an ALV/CGS-3 Platform-based Goniometer System equipped with an ALV-7004 correlator and an ALV/CGS-3 goniometer. An ALV Static and Dynamic Enhancer detection unit was used to detect the signal. The light source was the second harmonic of a diode-pumped Coherent Innova Nd:YAG laser ($\lambda = 532 \text{ nm}$), linearly polarized in the vertical direction. Cylindrical Hellma scattering cells were utilized, previously cleaned two times in deionized water and ethanol, and then dried with compressed air. The DLS equipment was used to study the sol–gel transition of 200 mm samples of **Res-Br**. In this case, three runs of 10 s were performed, keeping the same scattering angle (90°), and increasing the temperature by 1 $^{\circ}\text{C}$ at each measurement (starting $T: 20^{\circ}\text{C}$). The analysis continued until a clear correlation function was observed, indicating the dissolution of the gel network.

Statistical Analysis: Fiber diameter and recovery values of the compression tests reported in the Supporting Information are presented as mean \pm standard deviation. TEM/SEM image analysis was performed using ImageJ software. Statistical analysis of fiber diameters was based on the measurement of at least 1000 fibers.

Supporting Information

Supporting Information is available from the Wiley Online Library or from the author.

Acknowledgements

A.P. and L.S. contributed equally to this work. This research was funded by the European Research Council (ERC) through a Consolidator grant (FoldHalo, no. 307108) and a Proof-of-Concept grant (MINIRES, no. 789815) that were awarded to P.M.

Open Access Funding provided by Politecnico di Milano within the CRUI-CARE Agreement.

Conflict of Interest

The authors declare no conflict of interest.

Data Availability Statement

The data that support the findings of this study are available from the corresponding author upon reasonable request.

Keywords

bromination, elastomers, halogen bonding, peptides, resilin, self-assembly, supramolecular chemistry

Received: February 7, 2022

Revised: June 2, 2022

Published online: June 20, 2022

- [1] G. W. Gribble, *Environ. Chem.* **2015**, *12*, 396.
- [2] C. D. Murphy, *J. Appl. Microbiol.* **2003**, *94*, 539.
- [3] H. Birkedal, R. K. Khan, N. Slack, C. Broomell, H. C. Lichtenegger, F. Zok, G. D. Stucky, J. H. Waite, *ChemBioChem* **2006**, *7*, 1392.
- [4] R. M. S. Schofield, J. C. Niedbala, M. H. Nesson, Y. Tao, J. E. Shokes, R. A. Scott, M. J. Latimer, *J. Struct. Biol.* **2009**, *166*, 272.
- [5] A. Pizzi, C. Pigliacelli, G. Bergamaschi, A. Gori, P. Metrangolo, *Coord. Chem. Rev.* **2020**, *411*, 213242.
- [6] J. N. Sloand, T. E. Culp, N. M. Wonderling, E. D. Gomez, S. H. Medina, *Adv. Funct. Mater.* **2021**, *31*, 2170300.
- [7] A. Pizzi, C. Pigliacelli, A. Gori, N. Nonappa, O. Ikkala, N. Demitri, G. Terraneo, V. Castelletto, I. W. Hamley, F. B. Bombelli, P. Metrangolo, *Nanoscale* **2017**, *9*, 9805.
- [8] A. Bertolani, L. Pirrie, L. Stefan, N. Houbenov, J. S. Haataja, L. Catalano, G. Terraneo, G. Giancane, L. Valli, R. Milani, O. Ikkala, G. Resnati, P. Metrangolo, *Nat. Commun.* **2015**, *6*, 7574.
- [9] M. R. Scholfield, M. C. Ford, A.-C. C. Carlsson, H. Butta, R. A. Mehl, P. S. Ho, *Biochemistry* **2017**, *56*, 2794.
- [10] E. Danelius, H. Andersson, P. Jarvoll, K. Lood, J. Gräfenstein, M. Erdélyi, *Biochemistry* **2017**, *56*, 3265.
- [11] A.-C. C. Carlsson, M. R. Scholfield, R. K. Rowe, M. C. Ford, A. T. Alexander, R. A. Mehl, P. S. Ho, *Biochemistry* **2018**, *57*, 4135.
- [12] D. M. Ryan, S. B. Anderson, B. L. Nilsson, *Soft Matter* **2010**, *6*, 3220.
- [13] D. M. Ryan, T. M. Doran, S. B. Anderson, B. L. Nilsson, *Langmuir* **2011**, *27*, 4029.
- [14] D. S. Macpherson, S. A. McPhee, B. M. Zeglis, R. V. Ulijn, *ACS Biomater. Sci. Eng.* **2022**, *8*, 579.
- [15] D. Maiolo, A. Pizzi, A. Gori, L. Gazzera, N. Demitri, A. Genoni, F. Baggio, F. Moda, G. Terraneo, F. B. Bombelli, P. Metrangolo, G. Resnati, *ChemistryOpen* **2020**, *9*, 253.
- [16] D. Maiolo, A. Pizzi, A. Gori, G. Bergamaschi, C. Pigliacelli, L. Gazzera, A. Consonni, F. Baggio, F. Moda, F. B. Bombelli, P. Metrangolo, G. Resnati, *Supramol. Chem.* **2020**, *32*, 247.
- [17] G. Cavallo, P. Metrangolo, R. Milani, T. Pilati, A. Priimagi, G. Resnati, G. Terraneo, *Chem. Rev.* **2016**, *116*, 2478.
- [18] R. Balu, N. K. Dutta, A. K. Dutta, N. R. Choudhury, *Nat. Commun.* **2021**, *12*, 149.
- [19] G. Qin, X. Hu, P. Cebe, D. L. Kaplan, *Nat. Commun.* **2012**, *3*, 1003.
- [20] T. B. H. Schroeder, J. Houghtaling, B. D. Wilts, M. Mayer, *Adv. Mater.* **2018**, *30*, 1705322.
- [21] L. Li, K. L. Kiick, *ACS Macro Lett.* **2013**, *2*, 635.
- [22] J. Sun, J. Su, C. Ma, R. Göstl, A. Herrmann, K. Liu, H. Zhang, *Adv. Mater.* **2020**, *32*, 1906360.
- [23] K. Heise, E. Kontturi, Y. Allahverdiyeva, T. Tammelin, M. B. Linder, Nonappa, O. Ikkala, *Adv. Mater.* **2021**, *33*, 2004349.
- [24] L. Li, A. Mahara, Z. Tong, E. A. Levenson, C. L. McGann, X. Jia, T. Yamaoka, K. L. Kiick, *Adv. Healthcare Mater.* **2016**, *5*, 266.
- [25] P. E. Mikael, R. Udangawa, M. Sorci, B. Cress, Z. Shtein, G. Belfort, O. Shoseyov, J. S. Dordick, R. J. Linhardt, *Regen. Eng. Transl. Med.* **2019**, *5*, 362.
- [26] X. Hu, X.-X. Xia, S.-C. Huang, Z.-G. Qian, *Biomacromolecules* **2019**, *20*, 3283.
- [27] Y. Zhang, T. H. Tao, *Adv. Mater.* **2019**, *31*, 1905767.

- [28] W. Fang, A. Paananen, M. Vitikainen, S. Koskela, A. Westerholm-Parvinen, J. J. Joensuu, C. P. Landowski, M. Penttilä, M. B. Linder, P. Laaksonen, *Biomacromolecules* **2017**, *18*, 1866.
- [29] C. L. McGann, R. E. Akins, K. L. Kiick, *Biomacromolecules* **2016**, *17*, 128.
- [30] Y. Kim, E. E. Gill, J. C. Liu, *Biomacromolecules* **2016**, *17*, 2530.
- [31] S. Lv, D. M. Dudek, Y. Cao, M. M. Balamurali, J. Gosline, H. Li, *Nature* **2010**, *465*, 69.
- [32] E. Gazit, *Annu. Rev. Biochem.* **2018**, *87*, 533.
- [33] A. M. Tamburro, S. Panariello, V. Santopietro, A. Bracalello, B. Bochicchio, A. Pepe, *ChemBioChem* **2009**, *11*, 83.
- [34] B. M. Bulheller, A. J. Miles, B. A. Wallace, J. D. Hirst, *J. Phys. Chem. B* **2008**, *112*, 1866.
- [35] P. Chakraborty, Y. Tang, T. Yamamoto, Y. Yao, T. Guterman, S. Zilberzwige-Tal, N. Adadi, W. Ji, T. Dvir, A. Ramamoorthy, G. Wei, E. Gazit, *Adv. Mater.* **2020**, *32*, 1906043.
- [36] X. Du, J. Zhou, J. Shi, B. Xu, *Chem. Rev.* **2015**, *115*, 13165.
- [37] T. R. Jahn, O. S. Makin, K. L. Morris, K. E. Marshall, P. Tian, P. Sikorski, L. C. Serpell, *J. Mol. Biol.* **2010**, *395*, 717.
- [38] A. Pizzi, N. Demitri, G. Terraneo, P. Metrangolo, *CrystEngComm* **2018**, *20*, 5321.
- [39] C. Valery, M. Paternostre, B. Robert, T. Gulik-Krzywicki, T. Narayanan, J.-C. Dedieu, G. Keller, M.-L. Torres, R. Cherif-Cheikh, P. Calvo, F. Artzner, *Proc. Natl. Acad. Sci.* **2003**, *100*, 10258.
- [40] C. Baldock, A. F. Oberhauser, L. Ma, D. Lammie, V. Siegler, S. M. Mithieux, Y. Tu, J. Y. H. Chow, F. Suleman, M. Malfois, S. Rogers, L. Guo, T. C. Irving, T. J. Wess, A. S. Weiss, *Proc. Natl. Acad. Sci.* **2011**, *108*, 4322.
- [41] C. Tarabout, S. Roux, F. Gobeaux, N. Fay, E. Pouget, C. Meriadec, M. Ligeti, D. Thomas, M. IJsselstijn, F. Besselievre, D.-A. Buisson, J.-M. Verbavatz, M. Petitjean, C. Valery, L. Perrin, B. Rousseau, F. Artzner, M. Paternostre, J.-C. Cintrat, *Proc. Natl. Acad. Sci.* **2011**, *108*, 7679.
- [42] A. Gautieri, A. Milani, A. Pizzi, F. Rigoldi, A. Redaelli, P. Metrangolo, *J. Mol. Model.* **2019**, *25*, 124.
- [43] P. Metrangolo, F. Baldelli Bombelli, A. Pizzi, M. Linder, P. Mohammadi, EP3724209, **2019**.
- [44] M. J. Frisch, G. W. Trucks, H. B. Schlegel, G. E. Scuseria, M. A. Robb, J. R. Cheeseman, G. Scalmani, V. Barone, B. Mennucci, G. A. Petersson, H. Nakatsuji, M. Caricato, X. Li, H. P. Hratchian, A. F. Izmaylov, J. Bloino, G. Zheng, J. L. Sonnenberg, M. Hada, M. Ehara, K. Toyota, R. Fukuda, J. Hasegawa, M. Ishida, T. Nakajima, Y. Honda, O. Kitao, H. Nakai, T. Vreven, J. A. Montgomery, Jr., et al., *Gaussian, Inc. Wallingford CT* **2009**.
- [45] A. D. Becke, *J. Chem. Phys.* **1993**, *98*, 5648.
- [46] J. A. Maier, C. Martinez, K. Kasavajhala, L. Wickstrom, K. E. Hauser, C. Simmerling, *J. Chem. Theory Comput.* **2015**, *11*, 3696.
- [47] C. I. Bayly, P. Cieplak, W. Cornell, P. A. Kollman, *J. Phys. Chem.* **1993**, *97*, 10269.
- [48] M. Ibrahim, *J. Comput. Chem.* **2011**, *31*, 2967.
- [49] W. L. De Lano, *PyMOL Molecular Graphics System* **2002**.
- [50] W. Humphrey, A. Dalke, K. Schulten, *J. Mol. Graph.* **1996**, *14*, 33.
- [51] A. Gautieri, S. Vesentini, A. Redaelli, M. J. Buehler, *Int. J. Mater. Res.* **2009**, *100*, 921.
- [52] A. Gautieri, M. Beeg, M. Gobbi, F. Rigoldi, L. Colombo, M. Salmona, *Int. J. Mol. Sci.* **2019**, *20*, 4641.
- [53] M. T. Nelson, W. Humphrey, A. Gursoy, A. Dalke, L. V. Kalé, R. D. Skeel, K. Schulten, *Int. J. High Perform. Comput. Appl.* **1996**, *10*, 251.
- [54] M. J. Harvey, G. Giupponi, G. De Fabritiis, *J. Chem. Theory Comput.* **2009**, *5*, 1632.
- [55] F. Rigoldi, A. Gautieri, A. D. Vedove, A. P. Lucarelli, S. Vesentini, E. Parisini, *Proteins: Struct., Funct., Bioinf.* **2016**, *84*, 744.
- [56] F. Rigoldi, P. Metrangolo, A. Redaelli, A. Gautieri, *J. Biol. Chem.* **2017**, *292*, 7348.
- [57] M. Sztucki, T. Narayanan, *J. Appl. Crystallogr.* **2006**, *40*, s459.